The Astrophysical Journal Letters, 855:L30 (6pp), 2018 March 10 https://doi.org/10.3847/2041-8213/aab272

H^- Opacity and Water Dissociation in the Dayside Atmosphere of the Very Hot Gas Giant WASP-18b

Jacob Arcangeli[1], Jean-Michel Désert[1], Michael R. Line[2], Jacob L. Bean[3], Vivien Parmentier[4], Kevin B. Stevenson[5], Laura Kreidberg[6,7], Jonathan J. Fortney[8], Megan Mansfield[9], and Adam P. Showman[10]
[1] Anton Pannekoek Institute for Astronomy, University of Amsterdam, Science Park 904, 1098 XH Amsterdam, The Netherlands
[2] School of Earth & Space Exploration, Arizona State University, Tempe, AZ 85287, USA
[3] Department of Astronomy & Astrophysics, University of Chicago, 5640 S. Ellis Avenue, Chicago, IL 60637, USA
[4] Aix Marseille Univ, CNRS, LAM, Laboratoire d'Astrophysique de Marseille, Marseille, France
[5] Space Telescope Science Institute, 3700 San Martin Drive, Baltimore, MD 21218, USA
[6] Harvard-Smithsonian Center for Astrophysics, Cambridge, MA 02138, USA
[7] Harvard Society of Fellows, 78 Mt. Auburn Street, Cambridge MA 02138, USA
[8] Department of Astronomy and Astrophysics, University of California, Santa Cruz, CA 95064, USA
[9] Department of Geophysical Sciences, University of Chicago, 5734 S. Ellis Avenue, Chicago, IL 60637, USA
[10] Department of Planetary Sciences and Lunar and Planetary Laboratory, University of Arizona, Tucson, AZ 85721, USA
Received 2017 December 19; revised 2018 February 23; accepted 2018 February 26; published 2018 March 15

Abstract

We present one of the most precise emission spectra of an exoplanet observed so far. We combine five secondary eclipses of the hot Jupiter WASP-18b ($T_{\rm day} \sim 2900$ K) that we secured between 1.1 and 1.7 μm with the Wide Field Camera 3 instrument on board the *Hubble Space Telescope*. Our extracted spectrum (S/N = 50, $R \sim 40$) does not exhibit clearly identifiable molecular features but is poorly matched by a blackbody spectrum. We complement this data with previously published *Spitzer*/Infrared Array Camera observations of this target and interpret the combined spectrum by computing a grid of self-consistent, 1D forward models, varying the composition and energy budget. At these high temperatures, we find there are important contributions to the overall opacity from H^- ions, as well as the removal of major molecules by thermal dissociation (including water), and thermal ionization of metals. These effects were omitted in previous spectral retrievals for very hot gas giants, and we argue that they must be included to properly interpret the spectra of these objects. We infer a new metallicity and C/O ratio for WASP-18b, and find them well constrained to be solar ($[M/H] = -0.01 \pm 0.35$, C/O < 0.85 at 3σ confidence level), unlike previous work but in line with expectations for giant planets. The best-fitting self-consistent temperature–pressure profiles are inverted, resulting in an emission feature at 4.5 μm seen in the *Spitzer* photometry. These results further strengthen the evidence that the family of very hot gas giant exoplanets commonly exhibit thermal inversions.

Key words: planets and satellites: atmospheres – planets and satellites: gaseous planets

1. Introduction

Hot Jupiters are the easiest exoplanets to study because they are hot enough to have most or all of their atmospheric constituents in gas phase. From the growing number of known exoplanets, the population of very-hot hot Jupiters has emerged (Sudarsky et al. 2000). This subset spans a range of dayside temperatures from 2500 to 4600 K, with the hottest being as hot as the photosphere of a K-dwarf star (KELT-9b; Gaudi et al. 2017). These extreme planets are currently being discovered by ground-based surveys that focus on bright stars. Several important questions have emerged from the study of these highly irradiated planets, including the influence of stellar irradiation on their inflated radii and mass-loss rate, their atmospheric composition, and the frequency and origin of stratospheric thermal inversions.

Hubeny et al. (2003) first proposed the possibility of a bifurcation in the thermal structure of giant exoplanet atmospheres. Strong irradiation combined with efficient optical absorbers in the atmosphere (such as TiO and VO in gas phase) could cause an inversion layer in the temperature–pressure profile (Fortney et al. 2006, 2008; Burrows et al. 2008; Parmentier et al. 2015).

Recent observations of some of these extreme hot giants have revealed temperature inversions in their atmospheres (WASP-33 b: Haynes et al. 2015; WASP-121 b: Evans et al. 2017; WASP-18 b: Sheppard et al. 2017). Nevertheless, for all these studies, the retrieved metallicities and abundances are much higher than expected for a solar composition (e.g., VO 1000× solar for WASP-121 b, metallicity ∼300× solar with a C/O ∼ 1 for WASP-18 b). This is surprising for such massive gas giants, as their expected formation channels imply that their metallicities should be close to their host stars', as observed in their cooler counterparts (e.g., Kreidberg et al. 2014a; Benneke 2015; Line et al. 2016).

In this Letter, we argue that chemistry and opacity sources that are well known to operate at high temperatures from stellar astrophysics are key to the interpretation of very hot gas giant atmospheres. In particular, some of the primary sources of opacity on the daysides of these atmospheres will thermally dissociate at sufficiently low pressures and high temperatures. A second consideration is the effect of thermal ionization, whose electrons provide the seeds for bound–free and free–free interactions with atomic hydrogen that generate H^- opacity (see Section 3.2). While these effects are included in some models of very hot gas giants, in particular those that assume radiative–convective equilibrium, (e.g., Barman et al. 2001; Burrows et al. 2008; Fortney et al. 2008), their consequences for spectral retrieval have not yet been explored.

In this context, we present a new analysis and interpretation of observations obtained with the *Hubble Space Telescope* Wide Field Camera 3 (*HST* WFC3) and *Spitzer* Infrared Array Camera (IRAC) of the dayside emission spectrum of WASP-18b. WASP-18b (Hellier et al. 2009) is a 10 $10\,M_J$ planet that orbits a bright F6 host ($V_{\rm mag} = 9.3$) on a short period (0.94 days), and has an equilibrium temperature of 2700 K. In Section 2, we present the observations and data analysis. In Section 3, we discuss the effect of thermal dissociation and H^- opacities on the interpretation of this emission spectrum.

2. Observations and Data Reduction

2.1. Observations

Our team observed five secondary eclipses of WASP-18b with 24 orbits of the *HST* as part of a larger Treasury program (GO-13467), including a phase curve presented in a separate paper (J. Arcangeli et al. 2018, in preparation). We concentrate here on the secondary eclipse observations. The data were obtained with *HST*/WFC3, with the G141 grism, covering 1.1 to 1.7 μm, using the spatial scanning technique in both directions. Individual pixels in the spectrum reached a maximum flux level of 30,000 electrons, below 40% of full-well saturation, where the pixel response is linear.

The first two eclipses were taken using the 256 × 256 pixel subarray (SPARS10, NSAMP = 12, 74 s exposures); however, the spectrum was seen to leak outside of this subframe. Subsequent data used the 512 × 512 subarray (SPARS10, NSAMP = 16, 112 s exposures) with the same scan rate. We remove part of the second eclipse's final orbit, due to a loss of fine-guidance.

2.2. Data Reduction and Analysis

We developed a custom data reduction and analysis pipeline following the methods outlined in Kreidberg et al. (2014b). We first form subexposures from each full exposure by subtracting consecutive non-destructive reads. We calibrate the wavelength solution using a direct image taken at the start of each visit. We apply a wavelength-dependent flat-field correction and remove cosmic rays using a local median filter. We calculate the average sky background by masking the spectra on each subexposure, iteratively clipping outlier pixels. We finally apply an optimal extraction algorithm (Horne 1986) to maximize the signal-to-noise ratio (S/N) from each subexposure.

The reduced light curves are dominated by time-dependent systematics characteristic of *HST* observations. We parameterize these using the model-ramp technique with a single exponential in time and a linear visit-long slope. We remove the first orbit of each visit from our analysis. The second orbit is parameterized with a separate ramp amplitude. We compare the model-ramp technique with a common-mode correction and find we reach the same precision in each of the light curve fits.

We fit for the instrument systematics, the eclipse-depth, and eclipse time simultaneously for a total of 7 free parameters for each of the white-light curves. We then bin the data into 14 wavelength channels and fit again in each channel while maintaining the ramp timescale and eclipse time fixed to the white-light curve values. The remaining system parameters are fixed to literature values from Southworth et al. (2009). We combine the five extracted secondary eclipse spectra since we find that each are consistent within one sigma. The residuals from the white-light curve fits range from 1.05× to 2× the photon noise limit. The precision reached in the spectroscopic fits is less than 1.2× photon noise for each bin.

In order to estimate the errors on our fitted parameters and identify the degeneracies in the model we use a Markov Chain Monte Carlo (MCMC) approach using the open-source EMCEE code (Foreman-Mackey et al. 2013). We test convergence by employing the Gelmaan–Rubin diagnostic for each chain of 10,000 steps with 400 walkers. Our final precision on the spectroscopic eclipse depths is 20 ppm per wavelength bin in the combined spectrum, achieving an S/N of 50 at a resolution of $R \sim 40$, shown in Table 1. Our combined spectrum is consistent with Sheppard et al. (2017).

3. Results and Discussion

The combined WFC3 emission spectrum (show in Figure 1) does not exhibit spectral features expected from molecules such as H_2O or TiO. We complement the WFC3 emission spectrum with four *Spitzer*/IRAC data points already published (Nymeyer et al. 2011; Maxted et al. 2013), after ensuring that the system parameters are consistent, and we present below several scenarios to explain this combined spectrum.

3.1. Fitting a Blackbody Spectrum

We first test whether the WFC3 emission spectrum is consistent with a simple blackbody spectrum, which would be caused by an isothermal atmosphere over the pressures probed. We find a best-fit blackbody temperature of 2890 ± 47 K, using a PHOENIX stellar model of $T = 6400$ K, $\log g = 4.5$, and $[M/H] = 0.0$ for the star. However, this is a relatively poor fit to the data, with a reduced χ^2 of 3.1.

The *Spitzer*/IRAC photometric points at 3.5, 5.8, and 8.0 μm lie on the blackbody spectrum extrapolated from our WFC3 data, but the planet's flux at 4.5 μm is larger by 2σ, suggesting the presence of emission features (see Figure 1). In this wavelength range the dominant opacity sources are CO and H_2O, and spectral features would appear in emission only if the temperature–pressure profile of the atmosphere were inverted, and not isothermal. However, the lack of water spectral features at 1.4 μm could appear to be at odds with this conclusion. Previous studies have explained WASP-18b's spectrum with a high C/O ratio that can deplete the gas-phase water and remove its spectral features while allowing for a non-isothermal atmosphere (Sheppard et al. 2017). In the following section, we present an alternative explanation taking into account the key changes in opacity at these high temperatures, due to molecular dissociation, thermal ionization, and the presence of H^- ions, while requiring nominal solar metallicity and C/O.

3.2. Opacity Sources in Very Hot Gas Giant Exoplanet Atmospheres

The dominant opacity sources in the near-infrared for hot Jupiters are H_2O, CO, and metal hydrides and oxides. However, for the very-hot hot Jupiters ($T > 2500$ K), a significant fraction of water also thermally dissociates at low pressures (Parmentier & Crossfield 2017). In cool stellar photospheres with similar temperatures, large water absorption features can still be observed in their spectra as the increased pressure at the photosphere due to their higher surface gravities prevents dissociation (Kirkpatrick et al. 1993). However, hot Jupiters have lower surface gravities, and consequently

Table 1
Extracted Secondary Eclipse Spectrum, Including Photometric *Spitzer*/IRAC Points from Maxted et al. (2013) and Nymeyer et al. (2011) and Best-fit Model from Our Grid Retrieval, Convolved to the Resolution of the Data

Wavelengths (μm)	Fp/Fs (ppm)	Error (ppm)	Model (ppm)	Wavelengths (μm)	Fp/Fs (ppm)	Error (ppm)	Model (ppm)
1.140–1.173	775	20	805	1.436–1.469	1131	21	1140
1.173–1.206	874	20	870	1.469–1.501	1190	21	1187
1.206–1.239	908	20	883	1.501–1.534	1237	21	1192
1.239–1.271	908	19	917	1.534–1.567	1171	23	1221
1.271–1.304	940	19	959	1.567–1.600	1205	24	1245
1.304–1.337	989	20	986	3.6	3020	150	3081
1.337–1.370	1050	20	1043	4.5	3850	170	3601
1.370–1.403	1105	20	1077	5.8	3700	300	4043
1.403–1.436	1141	21	1108	8.0	4100	200	4512

Note. Eclipse depths and 1σ errors for *HST*/WFC3 were obtained using MCMC analysis on each of the spectroscopic light curves.

photospheres at lower pressures (around 0.1 bar for WASP-18 b), thus their spectra should be depleted in water beyond 2700 K. Carbon monoxide is harder to thermally dissociate, and should be present for temperatures below 4000 K, as expected in WASP-18b. Furthermore, while the cross-section of water increases, the line contrast weakens at higher temperatures (e.g., Burrows et al. 1997). Hence, it is inherently harder to identify spectral features of water at high temperatures.

Opacities from the negative hydrogen ion H^- are relevant at temperatures between 2500 and 8000 K (e.g., Pannekoek 1931; Chandrasekhar 1945; Lenzuni et al. 1991), hence they are important for very highly irradiated exoplanets (Figure 1). Atomic hydrogen is produced through thermal dissociation of molecular hydrogen at these high temperatures (e.g., Bell et al. 2017), along with electrons from the metal ionization (see Figure 2). Therefore, we argue that the hottest gas giants will show significant opacity from H^- ions on their daysides. We study the importance of H^- with planet mass and temperature in a companion paper (V. Parmentier et al. 2018, in preparation).

3.3. Atmospheric Modeling Including H^- Opacities and Molecular Dissociation

We produce a newly developed cloud-free grid of 1D self-consistent radiative–convective–thermochemical equilibrium models to interpret the data (ScCHIMERA, Self-consistent CHIMERA; Line et al. 2013). We use the Toon et al. (1989) two-stream source function technique under the hemispheric mean approximation to solve for the infrared radiative fluxes at each atmospheric layer combined with a convective adjustment scheme in the deeper atmosphere. The incident stellar flux is modeled as pure attenuation at a disk-averaged airmass of $1/\sqrt{3}$. The molecular, ion, and condensate abundances are derived using the NASA CEA2 Gibbs-free energy minimization routine (Gordon & McBride 1994) given the elemental abundances scaled from Lodders et al. (2009) via the metallicity, [*M/H*], and carbon-to-oxygen ratio, C/O, while accounting for the depletion of elements due to condensate rain-out. We implement the line-by-line cross-section database described in Freedman et al. (2008, 2014) with in the correlated-K "resort-rebin" framework described in Lacis & Oinas (1991), Mollière et al. (2015), and Amundsen et al. (2016) at a constant resolving power of 100 between 0.3 and 200 μm. The code has been validated against analytic solutions and agrees to within 3% and against the brown dwarf models of Marley et al. (2010). Bound–free and free–free opacities are taken from John (1988) and Bell & Berrington (1987), respectively. The grid is parameterized with a scaling factor to the stellar flux ($0.75 \leqslant f \leqslant 2.5$) to account for the unknown albedo and day-to-night heat transport (such that when $f = 1$ there is complete day–night redistribution and when $f = 2$ only the dayside re-radiates), the metallicity ($-1 < [M/H] < 2$), and carbon-to-oxygen ratio ($0.1 < \mathrm{C/O} < 10$ with finer sampling between 0.75 and 2). Parameter estimation is performed over the grid using the EMCEE package (Foreman-Mackey et al. 2013) via interpolation of the spectra along the grid dimensions, binned to the appropriate WFC3 and *Spitzer* resolution elements/profiles. The grid resolution is fine enough that interpolation errors are negligible.

We achieve a best fit with a reduced chi-squared of 2.0. We found that, when both H^- opacities and dissociation effects were not included, our retrievals were pushed to high C/O in order to explain the lack of water features, as seen in other studies (e.g., Sheppard et al. 2017). A pairs plot of the posterior distributions is shown in Figure 3. The metallicity is constrained to be solar ($[M/H] = -0.01 \pm 0.35$). A high C/O ratio is ruled out; we retrieve $\mathrm{C/O} < 0.85$ at 3σ confidence, also consistent with solar. Our retrieved value of $f = 2.03 \pm 0.08$ is consistent with minimal day–night redistribution expected for such a hot planet (Perez-Becker & Showman 2013) and is measured by Maxted et al. (2013).

3.4. WASP-18b's Atmospheric Metallicity, Composition, and Thermal Structure

We compare the retrieved metallicity of WASP-18b to the measured metallicities of solar system giants and exoplanets in Figure 4 and show that WASP-18b agrees with the expectation that the metallicities of the most massive planets should approach the metallicities of their host stars.

The tight constraint on metallicity, despite the absence of spectrally resolved molecular features, comes in part from the dependence of H^- on metal fraction. The ionization of metals is the dominant source of free electrons that generate H^- opacity in the atmosphere, and so there is a direct link between the H^- continuum level and the abundance of metals. In particular, this is driven by the abundance of metals that are the dominant sources of free electrons (Na, K, and Ca; Longstaff et al. 2017). However, the complex relationship between the chemistry and the temperature structure as well as their joint effects on the

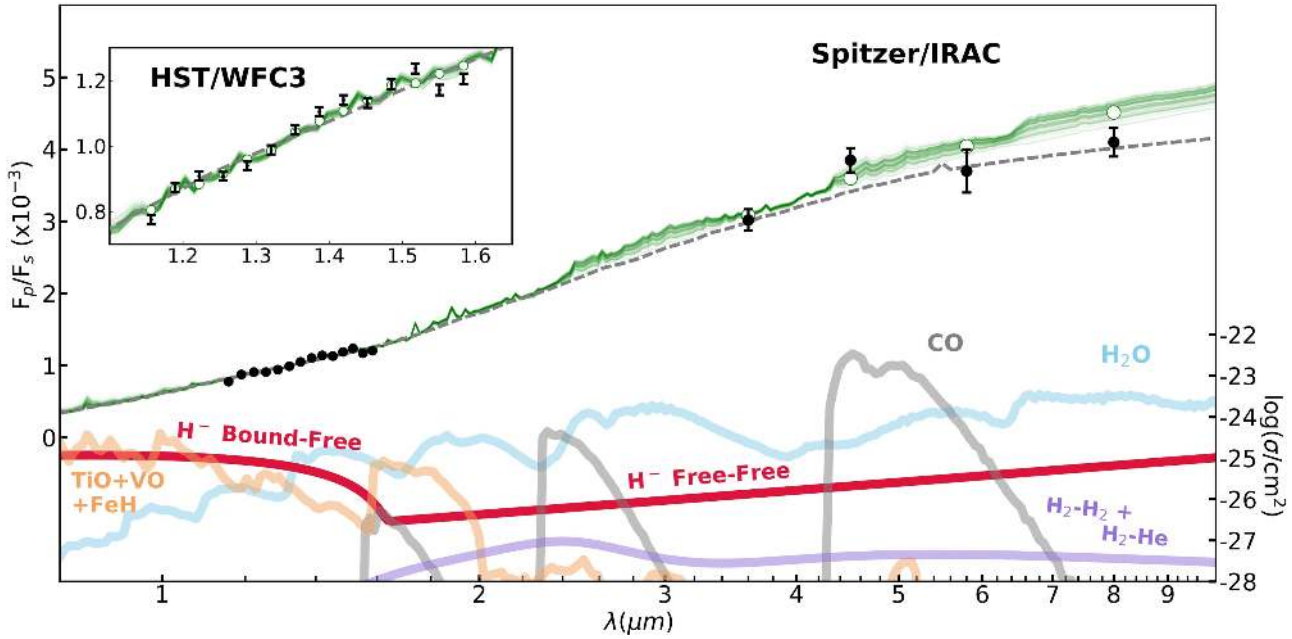

Figure 1. Dayside eclipse spectrum (black points) from this work and previous *Spitzer* observations compared to the best-fit model spectrum (white circles). The best-fit model has a reduced chi-squared of 2.0. In green are 100 samples from the posterior of the model spectrum derived from the grid retrieval, and in gray the best-fit blackbody spectrum to the WFC3 data of 2890 ± 47 K. Dominant opacity cross sections weighted by their molecular abundances (log(σ)) are shown for key molecules, taken at a pressure level of 0.33 bar (the peak of the WFC3 emission).

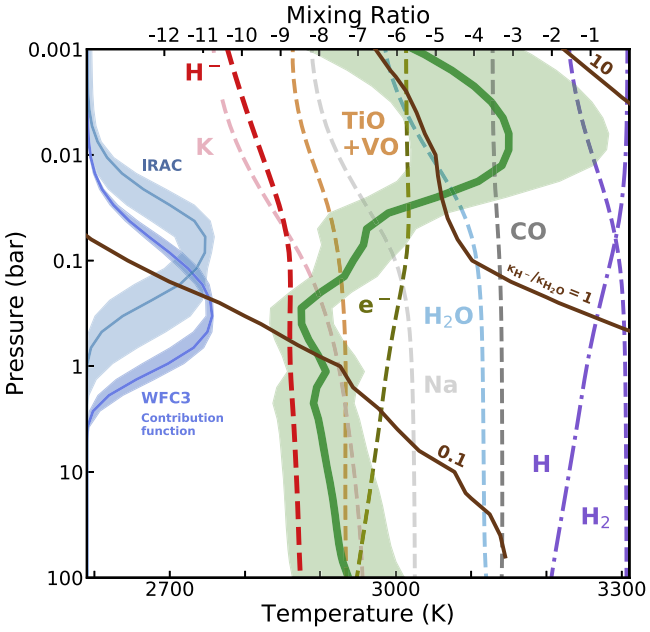

Figure 2. Best-fit *T*–*P* profile shown in green with 1σ error contours. Flux contribution functions are shown on the left for *HST*/WFC3 and *Spitzer*/IRAC in blue with 1σ regions. Dashed lines show the logarithm of the mixing ratios for key species at different pressures. Lines in brown denote contours of the ratio between the bound–free opacity of H$^-$ at 1.25 μm and molecular gas opacity, mainly from H_2O and TiO.

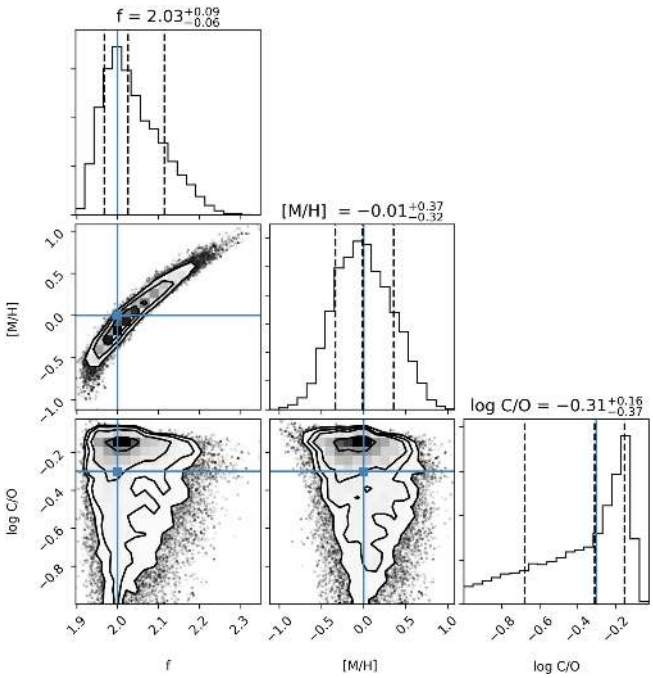

Figure 3. Posterior distributions from the grid retrieval. Forward models calculated varying log(C/O), [*M/H*], and *f* (redistribution factor). The extracted metallicity and C/O ratio are consistent with solar values (plotted in blue), *f* is consistent with no day–night redistribution.

spectrum make it difficult to attribute the retrieved metallicity solely to the H$^-$ continuum.

The nominal self-consistent temperature–pressure profiles (Figure 2) show a thermal inversion with temperature increasing with altitude at pressures between 0.1 and 0.01 bar. The inverted *T*–*P* profiles are also required to fit the emission feature at 4.5 μm, due to CO and H_2O, as observed with *Spitzer* (Nymeyer et al. 2011; Maxted et al. 2013). This inversion in our models is caused by high altitude absorption of optical stellar light by TiO and VO, and reduced cooling due to the dissociation of water. Vertical cold trapping of TiO can act to remove this species from the atmosphere of hot Jupiters (e.g., Désert et al. 2008), but not for planets with equilibrium temperatures above ∼1900 K (Parmentier et al. 2016). Horizontal cold trapping could still remove inversions from gas giants with high surface gravities (Parmentier et al. 2013;

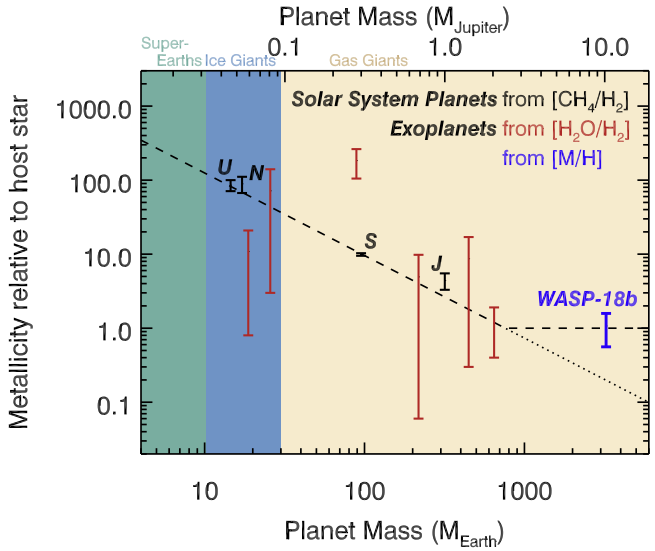

Figure 4. Mass–metallicity plot of the solar system planets including known exoplanet metallicity estimates from measured water abundances (M. Mansfield et al. 2018, in preparation and references therein). For the most massive planets, the metallicity should not follow a log-linear relationship but should approach the metallicity of the host star, as seen in WASP-18b where the stellar metallicity is 0.11 ± 0.08 (Torres et al. 2012).

Beatty et al. 2017); however, we do not see this in WASP-18b as our modeling favors an atmosphere with a TiO driven inversion. In order to test the presence of the inversion we perform a second grid retrieval, but with the opacities of TiO and VO removed. Practically, this removes the temperature inversion for the cases where the C/O < 0.8. For higher C/O, oxygen-poor atmospheres are naturally depleted in TiO/VO so they can no longer be the source of the inversion. By comparing the Bayesian Information Criterion (BIC) we found that the models including TiO and VO were favored (ΔBIC $= 6.5$) over those without, at odds with the retrieval by Sheppard et al. (2017). Even though TiO/VO are present in our model, their features are not seen in the WFC3 bandpass as they are damped by the H^- continuum while also being partially dissociated (seen in Figure 1). We finally compare the BIC between the best-fit model spectrum and the blackbody fit and find that the best-fit model to the combined *HST*/WFC3 and *Spitzer*/IRAC data is favored over the isothermal atmosphere (ΔBIC $= 12$). Hence, our best fit favors a dayside model atmosphere with a solar metallicity and C/O ratio, and with a thermal inversion.

The abundance of water in the atmosphere is expected to be partially depleted by dissociation (see Figure 2). While water is not dissociated at the pressure levels probed by the WFC3, dissociation of water higher in the atmosphere (below 0.1 bar) removes its emission feature at 1.4 μm. If dissociation were not present, the line center of emission would originate from higher in the atmosphere where the temperature is greater. We therefore attribute the the lack of water emission features both to an increased continuum opacity from H^- and to decrease in line opacity by dissociation of water higher in the atmosphere. The final spectrum between 1.1 and 1.7 μm therefore appears featureless as it is a sum of broad, partially depleted water emission at 1.4 μm and H^- bound–free opacity between 1.1 and 1.4 μm (see also V. Parmentier et al. 2018, in preparation). However, the dominant effect in the case of WASP-18b is the increased continuum opacity from H^- over the thermal dissociation of water (brown contours in Figure 2).

Another effect of water dissociation at low pressures is that it reduces the ability of the atmosphere to cool in this region (Mollière et al. 2015). Hence, in our models, even though the partial dissociation of TiO reduces the heating of the upper atmosphere, the atmospheric cooling efficiency remains lower than the heating efficiency, producing a thermal inversion.

4. Consequences for the Family of Very Hot Giant Exoplanets

Our results for WASP-18b have consequences for the new family of very hot gas giants, where extrapolation from cooler planets can be misleading (WASP-33 b: Haynes et al. 2015; WASP-103 b: Cartier et al. 2017; WASP-18 b: Sheppard et al. 2017; WASP-121 b: Evans et al. 2017). We find that the important impact of opacity both from H^- formed from metal ionization and from the reduced abundance of species, including water, due to thermal dissociation is key to the interpretation of very hot gas giant atmospheres. An evidence for this is that when including H^- opacity, the metallicity and C/O of WASP-18b are no longer super-solar, but drop to solar values. This is expected for typical formation scenarios of such a massive planet. Our result implies that the metallicity and C/O of other recently found metal-enriched very hot gas giants could also drop to solar values when H^- opacity is considered.

Interestingly, almost all of the very hot gas giants probed so far are best explained with the presence of a thermal inversion. Indeed, the primary diagnostic of these thermal inversions is a flux excess at 4.5 μm (Knutson et al. 2010). This implies that the hottest exoplanets exhibit a common behavior in their temperature structures, whose origin could be due to optical absorbers such as TiO/VO. Our modeling suggests that the WFC3 observations probe the region near the tropopause that is quasi-isothermal and appears to produce blackbody-like spectra due to the combined effects of dissociation and H^- opacity. Thus, we postulate that transition regions in classes of hot Jupiters could occur around temperatures near 2500 K (HAT-P-7 b; M. Mansfield et al. 2018, in preparation), below which H^- opacity becomes less significant, and near 1800 K, below which TiO and VO condense.

We thank Christiane Helling and Mickael Bonnefoy for useful discussions, and Eliza Kempton for providing feedback on the manuscript. J.M.D. acknowledges that the research leading to these results has received funding from the European Research Council (ERC) under the European Union's Horizon 2020 research and innovation programme (grant agreement No. 679633; Exo-Atmos). J.M.D. acknowledges support by the Amsterdam Academic Alliance (AAA) Program. Support for program GO-13467 was provided to the US-based researchers by NASA through a grant from the Space Telescope Science Institute, which is operated by the Association of Universities for Research in Astronomy, Inc., under NASA contract NAS 5-26555. J.L.B. acknowledges support from the David and Lucile Packard Foundation.

ORCID iDs

Michael R. Line https://orcid.org/0000-0002-2338-476X
Jacob L. Bean https://orcid.org/0000-0003-4733-6532
Vivien Parmentier https://orcid.org/0000-0001-9521-6258

Kevin B. Stevenson https://orcid.org/0000-0002-7352-7941
Laura Kreidberg https://orcid.org/0000-0003-0514-1147
Jonathan J. Fortney https://orcid.org/0000-0002-9843-4354
Megan Mansfield https://orcid.org/0000-0003-4241-7413

References

Amundsen, D. S., Mayne, N. J., Baraffe, I., et al. 2016, A&A, 595, A36
Barman, T. S., Hauschildt, P. H., & Allard, F. 2001, ApJ, 556, 885
Beatty, T. G., Madhusudhan, N., Tsiaras, A., et al. 2017, AJ, 154, 158
Bell, K. L., & Berrington, K. A. 1987, JPhB, 20, 801
Bell, T. J., Nikolov, N., Cowan, N. B., et al. 2017, ApJL, 847, L2
Benneke, B. 2015, arXiv:1504.07655
Burrows, A., Budaj, J., & Hubeny, I. 2008, ApJ, 678, 1436
Burrows, A., Marley, M., Hubbard, W. B., et al. 1997, ApJ, 491, 856
Cartier, K. M. S., Beatty, T. G., Zhao, M., et al. 2017, AJ, 153, 34
Chandrasekhar, S. 1945, ApJ, 102, 223
Désert, J.-M., Vidal-Madjar, A., Lecavelier Des Etangs, A., et al. 2008, A&A, 492, 585
Evans, T. M., Sing, D. K., Kataria, T., et al. 2017, Natur, 548, 58
Foreman-Mackey, D., Hogg, D. W., Lang, D., & Goodman, J. 2013, PASP, 125, 306
Fortney, J. J., Lodders, K., Marley, M. S., & Freedman, R. S. 2008, ApJ, 678, 1419
Fortney, J. J., Saumon, D., Marley, M. S., Lodders, K., & Freedman, R. S. 2006, ApJ, 642, 495
Freedman, R. S., Lustig-Yaeger, J., Fortney, J. J., et al. 2014, ApJS, 214, 25
Freedman, R. S., Marley, M. S., & Lodders, K. 2008, ApJS, 174, 504
Gaudi, B. S., Stassun, K. G., Collins, K. A., et al. 2017, Natur, 546, 514
Gordon, S., & McBride, B. J. 1994, Computer Program for Calculation of Complex Chemical Equilibrium Compositions and Applications. I. Analysis, Reference Publication RP-1311, Describes Theory and Numerical Algorithms Behind CEA Computer Program (Washington, DC: NASA), https://www.grc.nasa.gov/www/CEAWeb/RP-1311.htm
Haynes, K., Mandell, A. M., Madhusudhan, N., Deming, D., & Knutson, H. 2015, ApJ, 806, 146
Hellier, C., Anderson, D. R., Collier Cameron, A., et al. 2009, Natur, 460, 1098
Horne, K. 1986, PASP, 98, 609
Hubeny, I., Burrows, A., & Sudarsky, D. 2003, ApJ, 594, 1011
John, T. L. 1988, A&A, 193, 189
Kirkpatrick, J. D., Kelly, D. M., Rieke, G. H., et al. 1993, ApJ, 402, 643
Knutson, H. A., Howard, A. W., & Isaacson, H. 2010, ApJ, 720, 1569
Kreidberg, L., Bean, J. L., Désert, J.-M., et al. 2014a, ApJL, 793, L27
Kreidberg, L., Bean, J. L., Désert, J.-M., et al. 2014b, Natur, 505, 69
Lacis, A. A., & Oinas, V. 1991, JGR, 96, 9027
Lenzuni, P., Chernoff, D. F., & Salpeter, E. E. 1991, ApJS, 76, 759
Line, M. R., Stevenson, K. B., Bean, J., et al. 2016, AJ, 152, 203
Line, M. R., Wolf, A. S., Zhang, X., et al. 2013, ApJ, 775, 137
Lodders, K., Palme, H., & Gail, H.-P. 2009, LanB, 4, 44
Longstaff, E. S., Casewell, S. L., Wynn, G. A., Maxted, P. F. L., & Helling, C. 2017, MNRAS, 471, 1728
Marley, M. S., Saumon, D., & Goldblatt, C. 2010, ApJL, 723, L117
Maxted, P. F. L., Anderson, D. R., Doyle, A. P., et al. 2013, MNRAS, 428, 2645
Mollière, P., van Boekel, R., Dullemond, C., Henning, T., & Mordasini, C. 2015, ApJ, 813, 47
Nymeyer, S., Harrington, J., Hardy, R. A., et al. 2011, ApJ, 742, 35
Pannekoek, A. 1931, MNRAS, 91, 519
Parmentier, V., & Crossfield, I. 2017, arXiv:1711.07696
Parmentier, V., Fortney, J. J., Showman, A. P., Morley, C., & Marley, M. S. 2016, ApJ, 828, 22
Parmentier, V., Guillot, T., Fortney, J. J., & Marley, M. S. 2015, A&A, 574, A35
Parmentier, V., Showman, A. P., & Lian, Y. 2013, A&A, 558, A91
Perez-Becker, D., & Showman, A. P. 2013, ApJ, 776, 134
Sheppard, K. B., Mandell, A. M., Tamburo, P., et al. 2017, ApJL, 850, L32
Southworth, J., Hinse, T. C., Dominik, M., et al. 2009, ApJ, 707, 167
Sudarsky, D., Burrows, A., & Pinto, P. 2000, ApJ, 538, 885
Toon, O. B., McKay, C. P., Ackerman, T. P., & Santhanam, K. 1989, JGR, 94, 16287
Torres, G., Fischer, D. A., Sozzetti, A., et al. 2012, ApJ, 757, 161
Wakeford, H. R., Sing, D. K., Kataria, T., et al. 2017, Sci, 356, 628